PHYSICAL REVIEW FLUIDS **4**, 052401(R) (2019)

Rapid Communications

Hysteresis behavior in spanwise rotating plane Couette flow with varying rotation rates

Yuhan Huang,[1] Zhenhua Xia,[2,*] Minping Wan,[3] Yipeng Shi,[1] and Shiyi Chen[3,1,2,†]

[1]*State Key Laboratory for Turbulence and Complex Systems, College of Engineering, Peking University, Beijing 100871, China*

[2]*Department of Engineering Mechanics, Zhejiang University, Hangzhou 310027, China*

[3]*Department of Mechanics and Aerospace Engineering, Southern University of Science and Technology, Shenzhen 518055, China*

(Received 25 September 2018; published 14 May 2019)

The hysteresis behavior of spanwise rotating plane Couette flow is investigated by direct numerical simulations, where the simulations are carried out at a computational box $8\pi h \times 2h \times 4\pi h$ (here h is the half-channel height) along two opposite directions in rotation number ($\mathrm{Ro} = 2\Omega h/U_w$, with Ω the constant angular velocity in the spanwise direction and U_w half of the wall velocity difference) space. When rotation speed increases, structures with two pairs of roll cells appear in $0.02 \leqslant \mathrm{Ro} \leqslant 0.3$. However, structures with three pairs of roll cells are observed for $0.03 \leqslant \mathrm{Ro} \leqslant 0.3$ when Ro decreases from 0.5. Turbulent statistics on the two branches, such as the friction Reynolds number, turbulent kinetic energy, and kinetic energy from the secondary flows, exhibit similar hysteresis behaviors during $0.03 \leqslant \mathrm{Ro} \leqslant 0.3$. Intuitive discussions are also made to explain the hysteresis behavior.

DOI: 10.1103/PhysRevFluids.4.052401

Turbulence is a complex and chaotic system, where any slight perturbation in the initial field will cause a completely different instantaneous result after a long time. However, in the sense of statistics, the state of turbulence is usually thought to be irrelevant to initial conditions at very high Reynolds number [1,2]. The uniqueness of the turbulent state has not been proved strictly, but was generally accepted in turbulence research and modeling.

However, there was evidence that multiple states exist in both transition flows and fully developed turbulent flows. The phrase "multiple states" used here refers to turbulence with different statistical properties. In transitional flows, triggering of the transition from laminar to turbulence is believed to be sensitive to initial conditions [3,4]. For fully developed turbulence, multistate behavior was reported in von Kármán flow [5,6], Rayleigh-Bénard convection [7–9], rotating Rayleigh-Bénard convection [10–12], Rayleigh-Bénard convection with tilted containers [13], rotating spherical Couette flow [14], homogeneous sheared flow [15], forced rotating turbulence [16], Taylor-Couette flow (TCF) [17,18], and turbulent rotating plane Couette flow (RPCF) [19]. In some of these multistate cases, both states are stable and can exist independently for a long time [16,18–21], while in other cases, the state transition happens frequently [7]. Experiments of TCF [18,20] revealed that multiple states and hysteresis behavior exist even at $\mathrm{Re} \sim 10^6$. In their experiments, the shear stress was shown to be different under the same rotation speed but on different trajectories in phase space, and a hysteresis loop was observed in the plot of shear stress against rotation speed. In a later

*xiazh@zju.edu.cn

†chensy@sustc.edu.cn

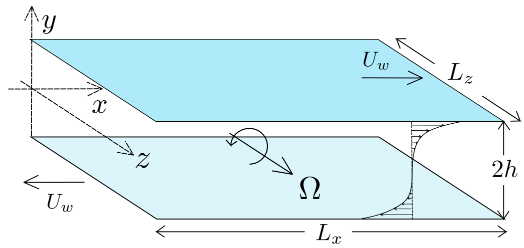

FIG. 1. Sketch of the numerical setup in RPCF [39].

experiment of TCF [21], the hysteresis behavior of system torque was investigated. The aspect ratio and boundary conditions were shown to have an effect on the hysteresis behavior.

Rotating plane Couette flow, as one of the benchmark problems for rotating wall-bounded turbulence [22], has been widely investigated in the past through both experiments and numerical simulations [19,23–39]. A sketch of the numerical setup is illustrated in Fig. 1, where the two planes, which are separated by $2h$, move in opposite directions with a constant velocity U_w. The system rotates in the z direction with a constant angular velocity Ω. It was shown that large-scale streamwise roll cells exist in RPCF and these secondary flows take a great share of the turbulent kinetic energy [35]. More recently, multiple states were reported in RPCF at $\mathrm{Ro} = 2\Omega h/U_w = 0.2$ with different initial flow fields [19]. It was observed that turbulent flows with two pairs of roll cells or three pairs of roll cells can both persist at a computational box of size $L_x \times L_y \times L_z = 10\pi h \times 2h \times 4\pi h$ for a very long time. However, whether multiple states can still exist with varying rotation rates is not clear.

In this paper, we explore the existence of multiple states in RPCF with varying rotation rates by changing the rotation number Ro in steps in two opposite directions in rotation number space. Each Ro step of computation uses the results from the last snapshot of a previous Ro step as the initial field. We aim to point out the parameter range where multiple states can persist and to confirm whether hysteresis behavior exists in RPCF. The related statistic properties will also be discussed.

The nondimensionalized governing equations for RPCF are

$$\frac{\partial u_k}{\partial x_k} = 0, \tag{1}$$

$$\frac{\partial u_i}{\partial t} + u_k \frac{\partial u_i}{\partial x_k} = -\frac{1}{\rho}\frac{\partial p}{\partial x_i} + \frac{1}{Re_w}\frac{\partial^2 u_i}{\partial x_k \partial x_k} + \mathrm{Ro}\varepsilon_{ik3}u_k, \tag{2}$$

where p is the effective pressure with the centrifugal force absorbed. The Reynolds number $\mathrm{Re}_w = U_w h/\nu$ (ν is the kinematic viscosity) and rotation number Ro are two control parameters. In the present work, $\mathrm{Re}_w = 1300$ is kept constant and an accurate Fourier-Chebyshev pseudospectral method is used to solve the governing equations with periodic boundary conditions in wall-parallel directions. The details about the numerical implementations can be found in Refs. [19,36]. The simulations[1] are run in two different groups, where the case for a particular Ro is initialized with the last flow field from the preceding simulation. In the first group (labeled group 1), Ro is increased in steps from 0.01 to 0.6. In the second group (labeled group 2), on the contrary, Ro is decreased from 0.5 to 0.01 with the same chosen Ro as group 1. The first case of each group starts from a laminar field imposed with divergence-free perturbations. (It is referred to as the laminar-perturbation initial field; see the Appendix for the detailed forms of the perturbation.) At each Ro, the simulation will evolve for a nondimensional time period $\Delta t^* = tU_w/h = 1250$, which is longer than most previous computations [24,25,34,36], to ensure that the flow achieves a statistically stationary state.

[1]The simulations were run on the TH-2A supercomputer in Guangzhou.

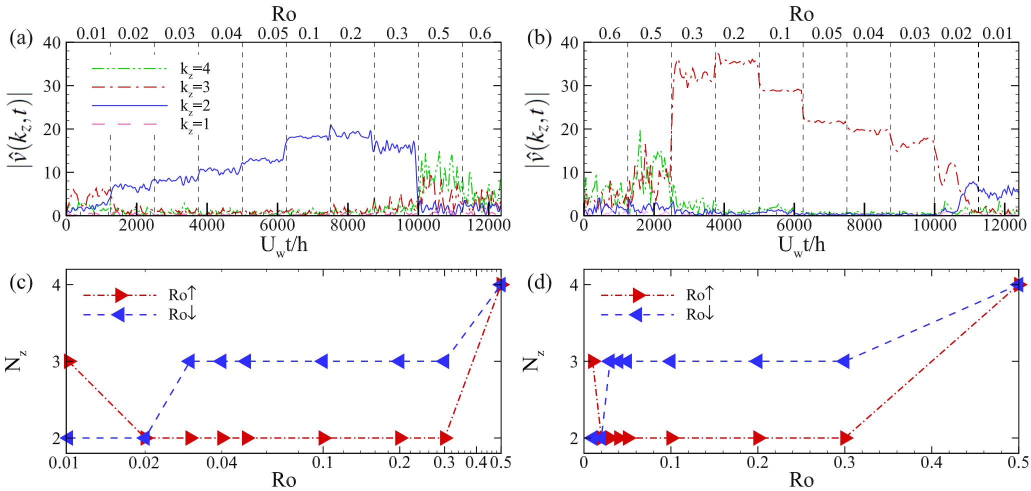

FIG. 2. Amplitude of the first four spanwise Fourier modes $|\hat{v}(k_z,t)|$ at the center plane from (a) group 1 and (b) group 2. The data between two vertical dashed lines in (a) and (b) represent the results at a constant rotation speed with the exact value of Ro shown on the top border. (c) and (d) Number of roll-cell pairs N_z represented by the order of the Fourier mode with maximum amplitude in the computation groups, where the horizontal axis in (c) is in logarithmic scale.

To give a more convincing analysis, an additional simulation is also carried out at $\mathrm{Ro} = 0.6$ with a laminar-perturbation initial field. After the same time duration $\Delta t^* = 1250$, Ro reduces to 0.5 and the simulation is run for another Δt^*. The flow statistics at $\mathrm{Ro} = 0.5$ are almost the same as those from the simulation started with a laminar-perturbation flow field. Thus, we could say that group 2 was started from $\mathrm{Ro} = 0.6$. In this work, the computational domain size and mesh resolutions are chosen to be $L_x \times L_y \times L_z = 8\pi h \times 2h \times 4\pi h$ and $256 \times 71 \times 256$. The maximum grid sizes in the wall-parallel plane are $\Delta_x^+ \approx 10.4$ and $\Delta_z^+ \approx 5.2$ in friction units at $\mathrm{Ro} = 0.1$ or 0.2 and the minimal values are $\Delta_x^+ \approx 8.34$ and $\Delta_z^+ \approx 4.17$ at $\mathrm{Ro} = 0.01$. The differences are about 20%. We have carried out a preliminary investigations on the effect of mesh resolution and computational domain size, and the results support the present choice of numerical setup [39].

In [19], Xia *et al.* reported the multiple states in RPCF where different pairs of large-scale roll cells were observed as in TCF [18]. This illustrates the importance of roll-cell structures. To provide an intrinsic view of the roll-cell structures, the wall-normal velocity at the center plane is investigated and a spanwise Fourier transform is performed:

$$|\hat{v}(k_z,t)| = \langle \mathscr{F}_z(v(x,0,z,t))\rangle_x.$$

Here $\mathscr{F}_z(f(z))$ stands for the discrete Fourier transform of $f(z)$ and $\langle f\rangle_x \equiv 1/L_x \int_0^{L_x} f(x)dx$ means the averaging operator in the x direction. Therefore, $|\hat{v}(k_z,t)|$ is actually the amplitude of the kth mode in the spanwise direction at time t, and k_z with maximum amplitude can be viewed as the number of roll-cell pairs.

Figures 2(a) and 2(b) display the time history of $|\hat{v}(k_z,t)|$ for $k = 1$–4 from groups 1 and 2, respectively. The data between two vertical dashed lines represent the results at a constant rotation speed with the exact value of Ro shown on the top border. For the simulations in group 1, the dominant mode is $k = 3$ at $\mathrm{Ro} = 0.01$. However, mode $k = 2$ becomes dominant when Ro increases to 0.02, and this dominant behavior persists until $\mathrm{Ro} = 0.5$, where mode $k = 4$ and mode $k = 3$ grow rapidly while mode $k = 2$ decays steeply. At the final part of the simulation, mode $k = 4$ persists while mode $k = 3$ decays, which makes mode $k = 4$ the dominant one. As Ro further increases to 0.6, mode $k = 4$ decays to the same level as modes $k = 2$ and $k = 3$, and

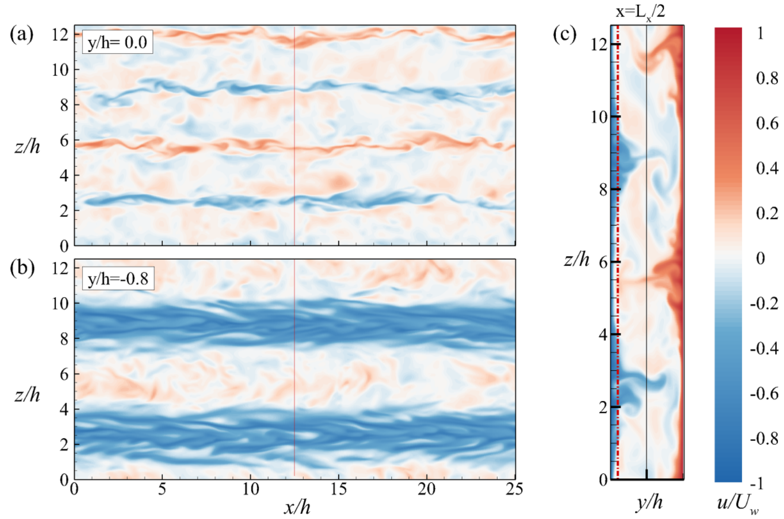

FIG. 3. Contours of streamwise velocity component u from an instantaneous flow field at Ro = 0.1 from group 1: (a) the x-z slice at $y = 0$, (b) the x-z slice at $y = -0.8h$, and (c) the y-z slice at $x = L_x/2$.

no dominant mode exists and the roll cells are believed to disappear. When the simulations are carried out following the setup in group 2, modes $k = 4$ and $k = 3$ first increase while modes $k = 1$ and $k = 2$ maintain a lower level. When the system rotates slower and Ro reduces to 0.3, mode $k = 4$ decays while mode $k = 3$ increases rapidly. When Ro continues to decrease, mode $k = 3$ keeps dominating over the other three modes while it begins to decay. At Ro = 0.02, mode $k = 3$ continues to decay while mode $k = 2$ begins to grow, and finally mode $k = 2$ becomes the dominant mode. At Ro = 0.01, the dominant mode is mode $k = 2$ as well.

The information about the roll cells displayed in Figs. 2(a) and 2(b) is mainly about the number N_z of roll-cell pairs in groups 1 and 2, respectively. This information is extracted and displayed in Figs. 2(c) and 2(d), and a hysteresis loop about the number of roll-cell pairs can be seen from it. This illustrates that multiple states do exist for a wide Ro range $0.02 < \text{Ro} < 0.5$. We would like to emphasize that Ro increases in steps in the present numerical setups, which may introduce disturbances on the initial flow field. Nevertheless, the flow problem can still persist the multiple states in this wide rotation number range, which makes the present observation more convincing. From this figure it can also be seen that the state with two pairs of roll cells is preferable when the system rotation accelerates and the state with three pairs of roll cells is preferable when the system rotates slower. It should be noticed that N_z depends on the spanwise box size L_z to a certain extent. If L_z increased to $6\pi h$, N_z might be 3 or 4 [39]. Since $L_z = 4\pi h$ is fixed in the present paper, we will use three-roll-cell-pair state and two-roll-cell-pair state to denote the different states.

In order to further characterize the flow differences, the flow structures are analyzed. Figures 3 and 4 show the contours of streamwise velocity component u from an instantaneous flow field at Ro = 0.1 from groups 1 and 2, respectively. All figures show three slices: Two of them are in the x-z plane at $y = 0$ (center plane, slice S1) and $y = -0.8h$ (slice S2), and the other is in the y-z plane at $x = 4\pi h$ (slice S3), which is located in the middle plane in the streamwise direction. It is apparent that the flow structures are quite different for these two simulations. For the simulation from group 1 as shown in Fig. 3, there are two pairs of large structures, which are characterized by the high-speed–low-speed streamwise striped contours of u at slice S1, and the high-speed–low-speed plumes from the top or bottom walls at slice S3. At slice S2 near the bottom wall, the two low-speed striped structures become wider. In RPCF, the counterrotating streamwise roll-cell structures can bring down higher-speed fluid from the top and bring up lower-speed fluid from

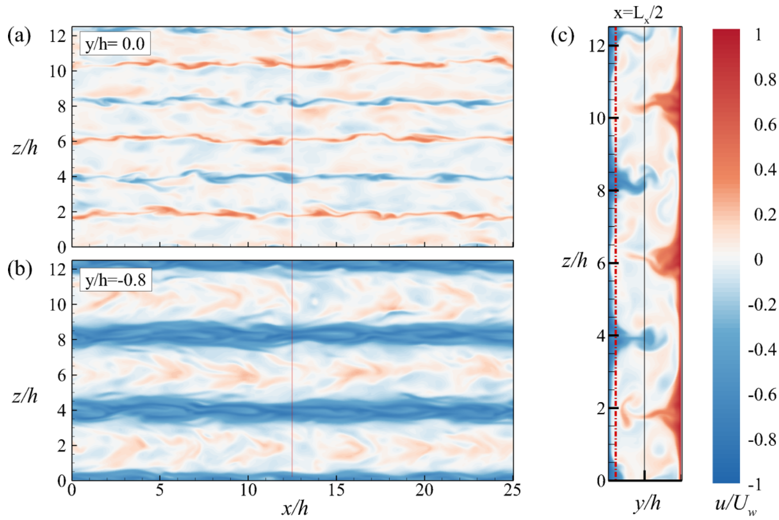

FIG. 4. Contours of streamwise velocity component u from an instantaneous flow field at $\mathrm{Ro} = 0.1$ from group 2: (a) the x-z slice at $y = 0$, (b) the x-z slice at $y = -0.8h$, and (c) the y-z slice at $x = L_x/2$.

the bottom. Combing the contours of u at three slices and the behaviors of roll cells, it can be inferred that only two pairs of roll cells exist in this simulation, which is consistent with the Fourier analysis shown in Fig. 2. On the other hand, for the simulation of group 2 at the same $\mathrm{Ro} = 0.1$, six high-speed–low-speed streamwise striped contours of u at slice S1 can be observed, while three obvious low-speed striped structures can be seen at slice S2. The striped structures are thinner than those from group 1, and the space between two adjacent ones is narrower too. From the figure, three pairs of roll cells can be inferred for this group. These flow structures are rather settled and they do not change during the simulations. The three-dimensional vorticity structures and the velocity vectors of the secondary flows (not shown here) also confirm the existences two different states. This scenario is quite similar to those reported by Huisman *et al.* [18] and van der Veen *et al.* [20]. In their works, they reported different turbulent states in TCF with a different number of turbulent Taylor vortices (rolls).

The different flow states will accompany different turbulent statistics. To analyze the statistical property of turbulence, a spatial-temporal averaging operator is adopted and the instantaneous flow field can be decomposed as

$$u_i(x, y, z, t) = \langle u_i \rangle(y) + u_i'(x, y, z, t).$$

Here $i = 1$, 2, or 3 refers to the x, y, and z directions, respectively (u, v, and w are used interchangeably with u_1, u_2, and u_3), and $\langle\cdot\rangle$ stands for the spatial-temporal averaging along x, z, and t. In the present analysis, the flow fields at the second half of the computation period in each stage, i.e., $625 \leqslant t^* \leqslant 1250$, are used to perform the flow statistics in order to avoid the interference of the flow transition due to the change of rotation number.

Following the above decomposition, we can obtain the profiles of mean velocity $\langle u \rangle$; three diagonal components of Reynolds stresses $\langle u'u' \rangle$, $\langle v'v' \rangle$, and $\langle w'w' \rangle$; Reynolds shear stress $-\langle u'v' \rangle$ (not shown here); the turbulent kinetic energy $k = (\langle u'u' \rangle + \langle v'v' \rangle + \langle w'w' \rangle)/2$; and thus the wall friction $\tau_w = \rho\nu d\langle u \rangle/dy|_{y/h=-1}$, the friction Reynolds number $\mathrm{Re}_\tau = u_\tau h/\nu$ ($u_\tau = \sqrt{\tau_w/\rho}$), and the volume-averaged turbulent kinetic energy $[k]$, where

$$[k] = \frac{1}{2h}\int_{-h}^{h} k(y)dy.$$

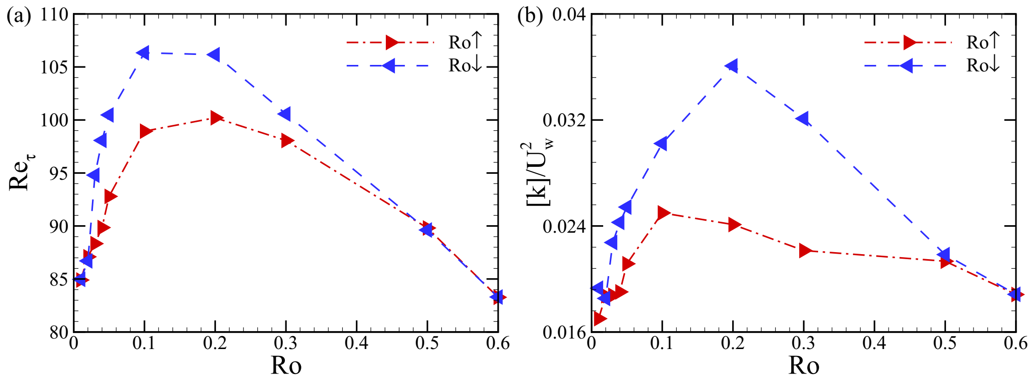

FIG. 5. (a) Friction Reynolds number Re_τ at different Ro from different groups. (b) Volume-averaged turbulent kinetic energy $[k]$ at different Ro from different groups.

Figure 5 shows Re_τ and $[k]$ (normalized by U_w^2) at different Ro from two groups, and clear hysteresis behavior can be observed for both quantities. For Re_τ as shown in Fig. 5(a), it follows the same trend in both groups, i.e., an increase at lower Ro and then a decrease at higher Ro, but its peak locations are different. In group 1, Re_τ reaches its maximum around $\mathrm{Ro} = 0.2$, where $\mathrm{Re}_{\tau,\max,1} \approx 100.3$. In group 2, the maximum $\mathrm{Re}_{\tau,\max,2} = 106.3$ is located around $\mathrm{Ro} = 0.1$. For $0.02 < \mathrm{Ro} < 0.5$, the values of Re_τ at the same Ro from two groups show a significant difference. The maximum deviation of Re_τ at the same Ro between the two groups is up to 9.1% at $\mathrm{Ro} = 0.04$. The values of Re_τ computed by Gai *et al.* [36] are very close to those from group 2 in our current computations. In their simulations, the computational time was not long enough and three pairs of roll cells were observed at the same L_z. The hysteresis behavior of Re_τ also implies the hysteresis behavior of the wall friction coefficient $C_f = \tau_w/\rho U_w^2$, since $C_f = (u_\tau/U_w)^2 = \mathrm{Re}_\tau^2/\mathrm{Re}_w^2$ and $\mathrm{Re}_w = 1300$ is fixed. From the behavior of Re_τ, it can be deduced that the wall friction from group 2 is much higher than that from group 1 for $0.02 < \mathrm{Ro} < 0.5$, which also means that stronger forces should be applied for group 2 in order to maintain the flow.

Figure 5(b) shows that the levels of turbulence intensities $[k]$ are also different at most Ro for groups 1 and 2. For group 1, the turbulent intensity increases with Ro until $\mathrm{Ro} \approx 0.1$ and then decreases with it. For group 2, the turbulent intensity generally follows the same trend but the maximum peak is located around $\mathrm{Ro} = 0.2$. The turbulence level from group 2 is generally higher than that from group 1 at the same Ro. The higher turbulence level should accompany a higher level of dissipation, and thus a higher value of external force that is used to drive the flow status, which is consistent with the trend of wall friction discussed above.

Now, we turn our attention to the roll cells. In order to identify the effects of the roll cell on the turbulence field, a triple-decomposition approach is applied to extract the secondary flows [24,36,40]. The decomposition is defined as

$$u_i(x, y, z, t) = \bar{u}_i(y, z) + u''(x, y, z, t) = \langle u_i\rangle(y) + u_i^s(y, z) + u''(x, y, z, t).$$

Here $\bar{u}_i$ stands for velocity averaged in the x and t directions, and $u_i^s(y, z) = \bar{u}_i(y, z) - \langle u_i\rangle(y)$ and u'' are usually called secondary flows and residual flows, respectively. The vectors (v^s, w^s) at the y-z plane can clearly show the secondary flow fields (not shown here; refer to [19,36]). Following the triple decomposition, we can define the kinetic energy from the secondary flows $k^s = 1/2\langle u_i^s u_i^s\rangle$ and the kinetic energy from the residual flows $k'' = 1/2\langle u_i'' u_i''\rangle$. It is easy to deduce that $k = k^s + k''$. Figure 6 shows the volume-averaged kinetic energy of the secondary flows $[k^s]$ (normalized by U_w^2), and again the hysteresis behavior can be observed. It is interesting to see that $[k^s]$ follows the same trend as $[k]$ when Ro changes. That is, the secondary flows first enhance with Ro increasing until it reaches its "optimal state" where its strength arrives at its maximum [41–43]. After that, a further

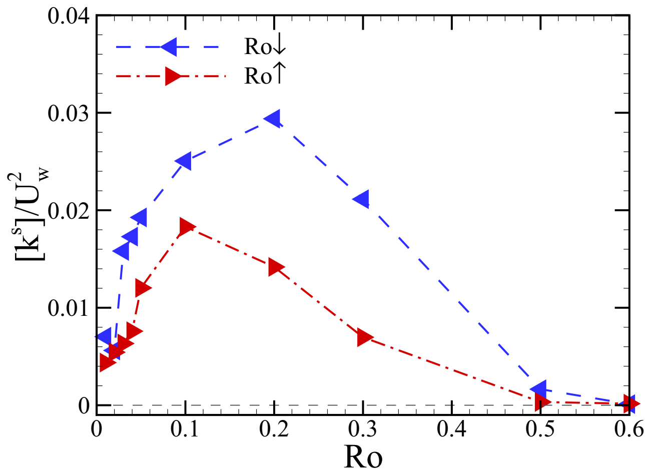

FIG. 6. Hysteresis behavior of the kinetic energy from the secondary flows.

increase of Ro will suppress the secondary flows due to the Taylor-Proudman effect [44,45]. More importantly, the values of $[k^s]$ from group 2 are generally larger than those from group 1 at the same Ro, which means that the secondary flows from group 2 are much stronger than those from group 1.

The hysteresis loops seem to close at Ro $= 0.02$ and 0.5 in the present study. At Ro $= 0.02$, there are two pairs of roll cells at $L_z = 4\pi h$. However, numerical studies in the past showed that there were three pairs of roll cells at the same L_z if the simulation was not run for a long enough time [36]. At this state, a slight mean counterflow was identified in the center region as observed in experiments [37]. In another work, we found that the three-roll-cell-pair state would emerge and evolve into a two-roll-cell-pair state if the simulation had run for long enough [39] and the counterflow also disappeared. At the present study, the two-roll-cell-pair state is easier to arrive at when the simulation started with a flow field at Ro $= 0.01$ or 0.03. At Ro $= 0.5$, the secondary flows are very weak and the roll cells might have lost their selectability power. At even higher Ro (e.g., Ro $= 0.6$), the secondary flows will disappear and no multiple state would exist.

Finally, we would like to discuss the hysteresis loops. Figure 7 shows the growth rate from the linear stability analysis by using the laminar linear velocity as the base flow at Ro $= 0.01$

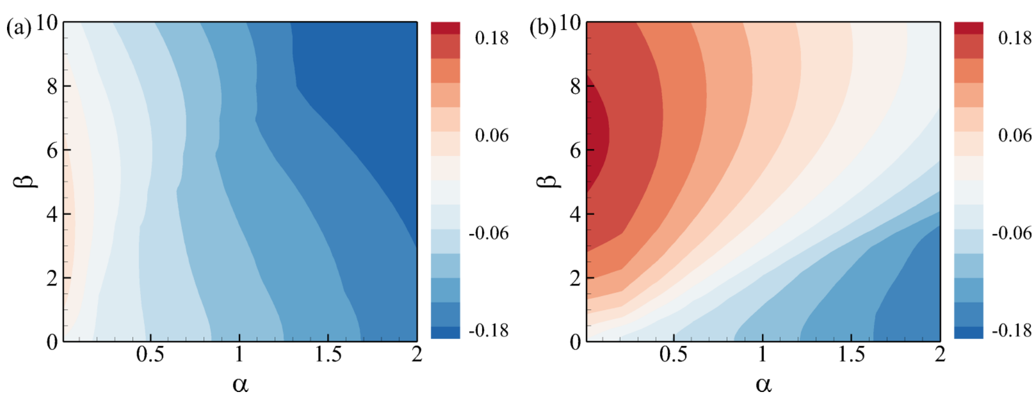

FIG. 7. Growth rate from the linear stability analysis by using the laminar linear velocity as the base flow at (a) Ro $= 0.01$ and (b) Ro $= 0.5$. Here α and β are the wave numbers in the streamwise and spanwise directions, respectively.

and 0.5. It is evident that the maximum growth rate occurs at $\alpha = 0$ for both cases. However, the corresponding spanwise wave numbers are different at these two rotation numbers. At Ro = 0.01, the most unstable spanwise wave number is around $\beta = 3.5$, while it is around $\beta = 6.5$ at Ro = 0.5. This is qualitatively consistent with the experimental observation that the size of the most preferable vortex becomes smaller when Ro increases [37] and the present direct numerical simulation (DNS) results. However, it should be noticed that the laminar linear base flow is quite different from the mean velocity in turbulent states. When the flow is at a turbulent state, the classic linear stability analysis with laminar linear velocity would lose its capability to interpret the flow phenomena. From our DNS results, there are four and three pairs of roll cells at the final turbulent state at Ro = 0.5 and 0.01, respectively, if the simulation is initialized with the laminar perturbation. At $0.03 \leqslant \text{Ro} \leqslant 0.3$, where the secondary flows are strong and the roll cells fill the channel in the wall-normal directions, the actual N_z can only be 2 or 3 due to the fixed spanwise domain size. If $N_z \geqslant 4$ [the ratio of width to height $(4\pi/2N_z)/2 \leqslant 0.785$], the roll cells would be elongated in the wall-normal direction and crowd each other, leading to the merging of roll cells. On the other hand, if $N_z = 1$, the ratio of width to height is $(4\pi/2N_z)/2 = \pi$ and the roll cells are stretched severely in the spanwise direction, resulting in the splitting of roll cells. At $N_z = 2$, the roll cells are also stretched in the spanwise direction with a much weaker stretch level and the splitting of roll cells is very difficult, since the turbulent kinetic energy at the three-roll-cell-pair state is much higher than that at the two-roll-cell-pair state, as shown in Fig. 5(b). From Fig. 2, the numbers of roll-cell pairs are more likely to stay unchanged when Ro increases or decreases in the range $0.03 \leqslant \text{Ro} \leqslant 0.3$. This present scenario is consistent with our previous finding that the "final" state of roll-cell structures is closely correlated with its initial condition [19] and it seems to be in favor of the conjecture by Huisman *et al.* [18] that the large-scale coherent structures and their selectability play a very important role in the multiple states of turbulence.

In summary, we performed two groups of direct numerical simulations of RPCF with the variations of Ro in opposite directions. Our results showed that multiple states exist for RPCF when $0.03 \leqslant \text{Ro} \leqslant 0.3$ and that clear hysteresis loops can be observed for turbulent statistics, such as the friction Reynolds number, turbulent kinetic energy, and kinetic energy from the secondary flows. The present results demonstrate that the multiple states in RPCF can exist for a wide range of rotation numbers.

This work was supported by the National Science Foundation of China (Grants No. 11822208, No. 11772297, No. 11672123, and No. 91752201).

APPENDIX

The perturbations added to the laminar flow field take the following forms:

$$u(x,y,z) = \varepsilon L_x \sin(\pi y)\left[\cos\left(\frac{2\pi x}{L_x}\right)\sin\left(\frac{2\pi z}{L_z}\right) + \frac{1}{2}\cos\left(\frac{4\pi x}{L_x}\right)\sin\left(\frac{2\pi z}{L_z}\right) + \cos\left(\frac{2\pi x}{L_x}\right)\sin\left(\frac{4\pi z}{L_z}\right)\right], \tag{A1}$$

$$v(x,y,z) = -\varepsilon[1+\cos(\pi y)]\left[\sin\left(\frac{2\pi x}{L_x}\right)\sin\left(\frac{2\pi z}{L_z}\right) + \sin\left(\frac{4\pi x}{L_x}\right)\sin\left(\frac{2\pi z}{L_z}\right) + \sin\left(\frac{2\pi x}{L_x}\right)\sin\left(\frac{4\pi z}{L_z}\right)\right], \tag{A2}$$

$$w(x,y,z) = -\frac{1}{2}\varepsilon L_z \sin(\pi y)\left[\sin\left(\frac{2\pi x}{L_x}\right)\cos\left(\frac{2\pi z}{L_z}\right) + \sin\left(\frac{4\pi x}{L_x}\right)\cos\left(\frac{2\pi z}{L_z}\right) + \frac{1}{2}\sin\left(\frac{2\pi x}{L_x}\right)\cos\left(\frac{4\pi z}{L_z}\right)\right]. \tag{A3}$$

Here ε is a constant that describes the amplitudes of the perturbations. In the current simulations, $\varepsilon = 0.005$. Similar perturbations were also used by Wang *et al.* [46].

---

[1] A. Kolmogorov, The local structure of turbulence in incompressible viscous fluid for very large Reynolds numbers, Dokl. Akad. Nauk SSSR **30**, 299 (1941) (In Russian).
[2] U. Frisch, *Turbulence* (Cambridge University Press, Cambridge, 1995).
[3] B. Eckhardt, T. M. Schneider, B. Hof, and J. Westerweel, Turbulence transition in pipe flow, Annu. Rev. Fluid Mech. **39**, 447 (2007).
[4] C. B. Lee and J. Z. Wu, Transition in wall-bounded flows, Appl. Mech. Rev. **61**, 030802 (2008).
[5] F. Ravelet, L. Marie, A. Chiffaudel, and F. Daviaud, Multistability and Memory Effect in a Highly Turbulent Flow: Experimental Evidence for a Global Bifurcation, Phys. Rev. Lett. **93**, 164501 (2004).
[6] P.-P. Cortet, A. Chiffaudel, F. Daviaud, and B. Dubrulle, Experimental Evidence of a Phase Transition in a Closed Turbulent Flow, Phys. Rev. Lett. **105**, 214501 (2010).
[7] H. Xi and K. Xia, Flow mode transitions in turbulent thermal convection, Phys. Fluids **20**, 055104 (2008).
[8] E. P. van der Poel, R. J. A. M. Stevens, and D. Lohse, Connecting flow structures and heat flux in turbulent Rayleigh-Bénard convection, Phys. Rev. E **84**, 045303(R) (2011).
[9] Y.-C. Xie, G.-Y. Ding, and K.-Q. Xia, Flow Topology Transition Via Global Bifurcation in Thermally Driven Turbulence, Phys. Rev. Lett. **120**, 214501 (2018).
[10] R. J. A. M. Stevens, J. Q. Zhong, H. J. H. Clercx, G. Ahlers, and D. Lohse, Transitions between Turbulent States in Rotating Rayleigh-Bénard Convection, Phys. Rev. Lett. **103**, 024503 (2009).
[11] S. Weiss, R. J. A. M. Stevens, J. Q. Zhong, H. J. H. Clercx, D. Lohse, and G. Ahlers, Finite-Size Effects Lead to Supercritical Bifurcations in Turbulent Rotating Rayleigh-Bénard Convection, Phys. Rev. Lett. **105**, 224501 (2010).
[12] P. Wei, S. Weiss, and G. Ahlers, Multiple Transitions in Rotating Turbulent Rayleigh-Bénard Convection, Phys. Rev. Lett. **114**, 114506 (2015).
[13] Q. Wang, Z. H. Wan, R. Yan, and D. J. Sun, Multiple states and heat transfer in two-dimensional tilted convection with large aspect ratios, Phys. Rev. Fluids **3**, 113503 (2018).
[14] D. S. Zimmerman, S. A. Triana, and D. P. Lathrop, Bi-stability in turbulent, rotating spherical Couette flow, Phys. Fluids **23**, 065104 (2011).
[15] K. P. Iyer, F. Bonaccorso, L. Biferale, and F. Toschi, Multiscale anisotropic fluctuations in sheared turbulence with multiple states, Phys. Rev. Fluids **2**, 052602 (2017).
[16] N. Yokoyama and M. Takaoka, Hysteretic transitions between quasi-two-dimensional flow and three-dimensional flow in forced rotating turbulence, Phys. Rev. Fluids **2**, 092602 (2017).
[17] B. Martínez-Arias, J. Peixinho, O. Crumeyrolle, and I. Mutabazi, Effect of the number of vortices on the torque scaling in Taylor-Couette flow, J. Fluid Mech. **748**, 756 (2014).
[18] S. G. Huisman, R. C. A. van der Veen, C. Sun, and D. Lohse, Multiple states in highly turbulent Taylor-Couette flow, Nat. Commun. **5**, 3820 (2014).
[19] Z. Xia, Y. Shi, Q. Cai, M. Wan, and S. Chen, Multiple states in turbulent plane Couette flow with spanwise rotation, J. Fluid Mech. **837**, 477 (2018).
[20] R. C. A. van der Veen, S. G. Huisman, O. Dung, H. L. Tang, C. Sun, and D. Lohse, Exploring the phase space of multiple states in highly turbulent Taylor-Couette flow, Phys. Rev. Fluids **1**, 024401 (2016).
[21] M. Gul, G. E. Elsinga, and J. Westerweel, Experimental investigation of torque hysteresis behavior of Taylor-Couette flow, J. Fluid Mech. **836**, 635 (2018).
[22] S. Jakirlić, K. Hanjalić, and C. Tropea, Modeling rotating and swirling turbulent flows: A perpetual challenge, AIAA J. **40**, 1984 (2002).
[23] K. H. Bech and H. I. Andersson, in *Direct and Large-Eddy Simulation I: Selected Papers from the First ERCOFTAC Workshop on Direct and Large-Eddy Simulation*, edited by P. R Voke, L. Kleiser, and J.-P. Chollet (Springer Netherlands, Dordrecht, 1994), pp. 13–24.

[24] K. H. Bech and H. I. Andersson, Secondary flow in weakly rotating turbulent plane Couette flow, J. Fluid Mech. **317**, 195 (1996).

[25] K. H. Bech and H. I. Andersson, Turbulent plane Couette flow subject to strong system rotation, J. Fluid Mech. **347**, 289 (1997).

[26] K. H. Bech and H. I. Andersson, Growth and decay of longitudinal roll cells in rotating turbulent plane Couette flow, in *Advances in Turbulence VI*, edited by S. Gavrilakis, L. Machiels, and P. A. Monkewitz (Kluwer, Dordrecht, 1996), pp. 91–94.

[27] K. Bech, N. Tillmark, P. H. Alfredsson, and H. I. Andersson, An investigation of turbulent plane Couette flow at low Reynolds numbers, J. Fluid Mech. **286**, 291 (1995).

[28] T. Tsukahara, H. Kawamura, and K. Shingai, DNS of turbulent Couette flow with emphasis on the large-scale structure in the core region, J. Turbul. **7**, N19 (2006).

[29] K. Hiwatashi, P. H. Alfredsson, N. Tillmark, and M. Nagata, Experimental observations of instabilities in rotating plane Couette flow, Phys. Fluids **19**, 048103 (2007).

[30] T. Tsukahara, N. Tillmark, and P. H. Alfredsson, Flow regimes in a plane Couette flow with system rotation, J. Fluid Mech. **648**, 5 (2010).

[31] M. Barri and H. I. Andersson, Computer experiments on rapidly rotating plane Couette flow, Commun. Comput. Phys. **7**, 683 (2010).

[32] T. Tsukahara, Structures and turbulent statistics in a rotating plane Couette flow, J. Phys.: Conf. Ser. **318**, 022024 (2011).

[33] A. Suryadi, N. Tillmark, and P. H. Alfredsson, Velocity measurements of streamwise roll cells in rotating plane Couette flow, Exp. Fluids **54**, 1617 (2013).

[34] M. Salewski and B. Eckhardt, Turbulent states in plane Couette flow with rotation, Phys. Fluids **27**, 045109 (2015).

[35] J. Gai, Z. Liu, J. Luo, Q. Cai, and Z. Xia, Penta-decomposition of instantaneous field in spanwise-rotating turbulent plane Couette flows, Acta Phys. Sin. **65**, 244703 (2016) (In Chinese).

[36] J. Gai, Z. Xia, Q. Cai, and S. Chen, Turbulent statistics and flow structures in spanwise-rotating turbulent plane Couette flows, Phys. Rev. Fluids **1**, 054401 (2016).

[37] T. Kawata and P. H. Alfredsson, Turbulent rotating plane Couette flow: Reynolds and rotation number dependency of flow structure and momentum transport, Phys. Rev. Fluids **1**, 034402 (2016).

[38] T. Kawata and P. H. Alfredsson, Experiments in rotating plane Couette flow: Momentum transport by coherent roll-cell structure and zero-absolute-vorticity state, J. Fluid Mech. **791**, 191 (2016).

[39] Y. Huang, Z. Xia, M. Wan, Y. Shi, and S. Chen, Numerical investigation of plane Couette flow with weak spanwise rotation, Sci. China Phys. Mech. Astron. **62**, 044711 (2019).

[40] R. D. Moser and P. Moin, The effects of curvature in wall-bounded turbulent flows, J. Fluid Mech. **175**, 479 (1987).

[41] D. P. M. van Gils, S. G. Huisman, S. Grossmann, C. Sun, and D. Lohse, Optimal Taylor-Couette turbulence, J. Fluid Mech. **706**, 118 (2012).

[42] R. Ostilla-Mónico, R. J. A. M. Stevens, S. Grossmann, R. Verzicco, and D. Lohse, Optimal Taylor-Couette flow: Direct numerical simulations, J. Fluid Mech. **719**, 14 (2013).

[43] R. Ostilla-Mónico, S. G. Huisman, T. J. G. Jannink, D. P. M. Van Gils, R. Verzicco, S. Grossmann, C. Sun, and D. Lohse, Optimal Taylor-Couette flow: Radius ratio dependence, J. Fluid Mech. **747**, 1 (2014).

[44] P. K. Kundy, I. M. Cohen, D. R. Dowling, and G. Tryggvason, *Fluid Mechanics* (Academic, New York, 2015), p. 771.

[45] S. Grossmann, D. Lohse, and C. Sun, High-Reynolds number Taylor-Couette turbulence, Annu. Rev. Fluid Mech. **48**, 53 (2016).

[46] L.-P. Wang, C. Peng, Z. Guo, and Z. Yu, Lattice Boltzmann simulation of particle-laden turbulent channel flow, Comput. Fluids **124**, 226 (2016).